

# Bayesian estimation of non-linear centroid moment tensors using multiple seismic data sets

Mahdi Hamidbeygi<sup>1</sup>, Hannes Vasyura-Bathke<sup>2,3</sup>, Jan Dettmer<sup>1</sup>, David W. Eaton<sup>1</sup> and Stan E. Dosso<sup>4</sup>

<sup>1</sup>Department of Geoscience, University of Calgary, Calgary, AB T2N 1N4, Canada. E-mail: [mahdihamidbeygi@gmail.com](mailto:mahdihamidbeygi@gmail.com)

<sup>2</sup>Institute for Geosciences, University of Potsdam, 14476 Potsdam, Germany

<sup>3</sup>Now at: Helmholtz Centre Potsdam, German Research Centre for Geosciences GFZ, 14473 Potsdam, Germany

<sup>4</sup>School of Earth and Ocean Sciences, University of Victoria, Victoria, BC V8P 3E6, Canada

Accepted 2023 September 26. Received 2023 September 25; in original form 2022 October 20

## SUMMARY

Centroid moment tensor (CMT) parameters of earthquakes are routinely estimated to gain information on structures and regional tectonics. However, for small earthquakes ( $M < 4$ ), it is still challenging to determine CMTs due to the lack of high-quality waveform data. In this study, we propose to improve solutions for small earthquakes by incorporating multiple seismic data types in Bayesian joint inversion: polarities picked on broad-band signals, amplitude spectra for intermediate frequency bands (0.2–2.0 Hz), and waveforms at low frequencies (0.05–0.2 Hz). Both measurement and theory errors are accounted for by iterative estimation of non-Toeplitz covariance matrices, providing objective weightings for the different data types in the joint parameter estimation. Validity and applicability of the method are demonstrated using simulated and field data. Results demonstrate that combinations of data, such as a single high-quality waveform, a few amplitude spectra and many waveform polarities, are able to resolve CMT parameters to comparable quality as if many high-quality waveforms were available. Results of 10 induced seismic events that occurred in northeastern British Columbia, Canada, between January 2020 and February 2022 indicate predominantly strike-slip focal mechanisms with low non-double-couple components. These events appear to be located at shallow depths with short time duration, as expected for induced seismicity. These results are consistent with previous studies, indicating that this method reduces the dependence of source inversion on high-quality waveforms, and can provide resolution of CMT parameters for earthquakes as small as  $M_L$  1.6.

**Key words:** Computational seismology; Earthquake source observation; Induced seismicity; Statistical seismology; Bayesian joint inference.

## 1 INTRODUCTION

Centroid moment tensors (CMTs) are point-source approximations for earthquake ruptures and provide important source characteristics (Dziewonski *et al.* 1981). Point-source approximations can be considered when the earthquake source dimension and duration are small relative to the wavelength and period of the observed seismic wavefield. CMT inversions have been primarily useful for interpreting the style of faulting and deformation in active tectonic settings, as well as providing source characteristics for other studies, for example tomography (Valentine & Woodhouse 2010). In addition, understanding fault orientations and mechanisms can constrain the stress field in a region (Vavryčuk 2014). Even though the point

source approximation simplifies rupture significantly, inferring all CMT parameters remains a challenging inverse problem.

The challenges in the inverse problem are closely related to the parametrization of the full CMT (Stähler & Sigloch 2014), which includes the moment tensor, the centroid, and the source–time function (STF). The moment tensor comprises six force couples such that linear and angular momentum are conserved. The centroid of the rupture is parametrized by latitude, longitude, depth and time. Finally, the time dependence of moment release, the STF, can be considered as unknown and parametrized in various ways. From the force couples, source characteristics such as magnitude and fault plane orientation can be computed, albeit with uncertainty. Estimating centroid and STF causes numerical challenges due to non-

linearities (e.g. Stähler & Sigloch 2014; Cesca *et al.* 2016; Vasyura-Bathke *et al.* 2021). Therefore, many studies assume the source type to be pure shear slip, described by a four-parameter moment tensor (a double-couple mechanism) and centroid and source–time function are assumed to be known.

Various data types have been employed individually and jointly to estimate CMTs. Most commonly, seismic waveforms (e.g. Zhao & Helmberger 1994; Wéber 2006; Herrmann *et al.* 2011; Ekström *et al.* 2012; Stähler & Sigloch 2014; Mustać & Tkalčić 2016; Fichtner & Simutè 2018) and first-motion polarity data (e.g. Brillinger *et al.* 1980; Hardebeck & Shearer 2002; Snoke *et al.* 2003; Walsh *et al.* 2009) have been used. In addition, amplitude spectra (e.g. Cesca *et al.* 2006; Fox *et al.* 2012), amplitude ratios (e.g. Hardebeck & Shearer 2003; Pugh *et al.* 2016; Shang & Tkalčić 2020) and geodetic data (e.g. Heimann *et al.* 2018; Vasyura-Bathke *et al.* 2020) have been considered for MTs. Each data type has limitations and jointly inverting multiple types with complementary information is desirable (e.g. De Matteis *et al.* 2016; Pugh *et al.* 2016; Heimann *et al.* 2018; Kühn *et al.* 2020; Petersen *et al.* 2021). For example, waveforms can be reliably modelled between 0.01 and 0.5 Hz for typical 1-D layered earth models at large distances, depending on the magnitudes of events, assuming that the point source assumption is valid and that structural effects other than layering are small. More detailed earth models can be employed at small epicentral distances of a few kilometres to permit Green’s function computations at higher frequencies. Therefore, the availability of high-quality waveforms at stations near the epicentre is important, but often only a few such waveforms exist. First-motion polarity data are picked on broad-band seismograms and include information from higher frequencies. The main disadvantage of polarity data is that their binary nature discards much information, resulting in these data only constraining the focal mechanism. Amplitude spectra can be reliably modelled at higher frequencies than possible for waveforms (Cesca *et al.* 2010) since phase information is discarded. Finally, spectra retain more information than polarities. Therefore, the three data types contain complementary information.

Since the CMT inverse problem is non-unique and non-linear (e.g. Stähler & Sigloch 2014; Cesca *et al.* 2016; Vasyura-Bathke *et al.* 2021), parameter estimation should include uncertainty quantification to permit meaningful interpretation of results. The uncertainties are caused by data errors that include measurement and theory errors (Tarantola *et al.* 1982) and require particularly careful consideration in joint inversion since the errors for various data types govern how these data contribute to the CMT solution. Bayesian inference is an effective tool to rigorously treat data errors in the inversion (e.g. Malinverno & Briggs 2004; Monelli & Mai 2008; Razafindrakoto & Mai 2014; Vasyura-Bathke *et al.* 2021), thereby appropriately weighting the data types. Bayesian inversion has been extensively applied to moment tensor inversion (e.g. Wéber 2006; Mustać & Tkalčić 2016; Gu *et al.* 2018), although fewer works consider the full CMT (e.g. Stähler & Sigloch 2014; Vasyura-Bathke *et al.* 2020). The most common inversion methods that characterize uncertainty of source parameters utilize a single or a combination of two data sets among first-motion polarities, amplitude ratios, and time- or frequency-domain traces (e.g. Walsh *et al.* 2009; De Matteis *et al.* 2016; Pugh *et al.* 2016; Alvizuri & Tape 2016; Vackář *et al.* 2017; Gu *et al.* 2018; Heimann *et al.* 2018; Wéber 2018; Shang & Tkalčić 2020; Kühn *et al.* 2020; Petersen *et al.* 2021).

In this work, we present a Bayesian joint inversion method for small earthquakes with local magnitude ( $M_L$ ) less than 4 based

on first-motion polarities, amplitude spectra and waveforms. The method is implemented as a new feature of the Bayesian Earthquake Analysis Tool (Vasyura-Bathke *et al.* 2020). To improve the ability to resolve CMT parameters for small events, we utilize waveforms at low frequencies (0.05–0.2 Hz), spectra at intermediate frequencies (0.3–1.2 Hz) and polarities picked on broad-band seismograms (Fig. 1). The novelty in the approach presented here is the fully non-linear treatment by considering source time function and centroid parameters such as time and location for small earthquakes, and the combined empirical and hierarchical covariance estimation while using the previously mentioned data types jointly in a rigorous Bayesian framework. In addition, the weighting issues in joint inversion have been taken care of objectively in previous works while the data sets are weighted by their covariance matrix in our presented method. These are shown to permit resolving source parameters with limited data availability to comparable quality as if extensive high-quality data were available. This method permits estimating smaller earthquake centroid parameters in regions where other methods require high-quality data. We apply our method to simulated and field data to evaluate its applicability and reliability. The events considered range from  $M$  1.6 to 4.2 and are induced by hydraulic fracturing operations in NE British Columbia, Canada. We present the results of 10 induced earthquakes, including the 30 November 2018,  $M_w$  4.2 earthquake near Fort St John, Canada.

## 2 METHOD

### 2.1 Bayesian inference

To study rupture characteristics, we assume earthquakes as point sources parametrized by the CMT. The parameters of the CMT include the moment tensor (MT) parameters in the lune parametrization (Tape & Tape 2015), centroid location (latitude, longitude, depth and centroid time) and source duration. The lune representation (MTQT) is a uniform parametrization of moment tensors (Tape & Tape 2015) particularly useful to specify prior distributions for parameters in Bayesian inference. Instead of representing the MT as force couples in units of Newton metres, MTQT represents a unit source by a focal mechanism with strike, dip and rake angles, and two parameters that describe the source type on the lune. We scale the unit source by the scalar moment. Specifying priors for focal mechanism angles and the source type is straightforward when compared to specifying priors for force couples. For example, the parametrization can be constrained to source types of interest, such as double-couple or deviatoric, without requiring proposed sets of force couples to meet the MT requirements for a particular source type. In addition, geological prior knowledge about strike or dip of known faults can be incorporated in the analysis with full CMTs.

In Bayesian inference, model parameters are random variables, and the sampling produces an ensemble of parameter vectors that approximates the posterior probability density (PPD) given data and prior information. The PPD can provide uncertainty estimates and other metrics of interest for individual parameters by marginalization. Bayes’ theorem relates the PPD  $p(\mathbf{m}|\mathbf{d})$  to the likelihood function  $L(\mathbf{m})$  which represents data information, and the prior  $p(\mathbf{m})$  which represents information about the model that is independent of the data as

$$p(\mathbf{m}|\mathbf{d}) \propto p(\mathbf{m})L(\mathbf{m}). \quad (1)$$

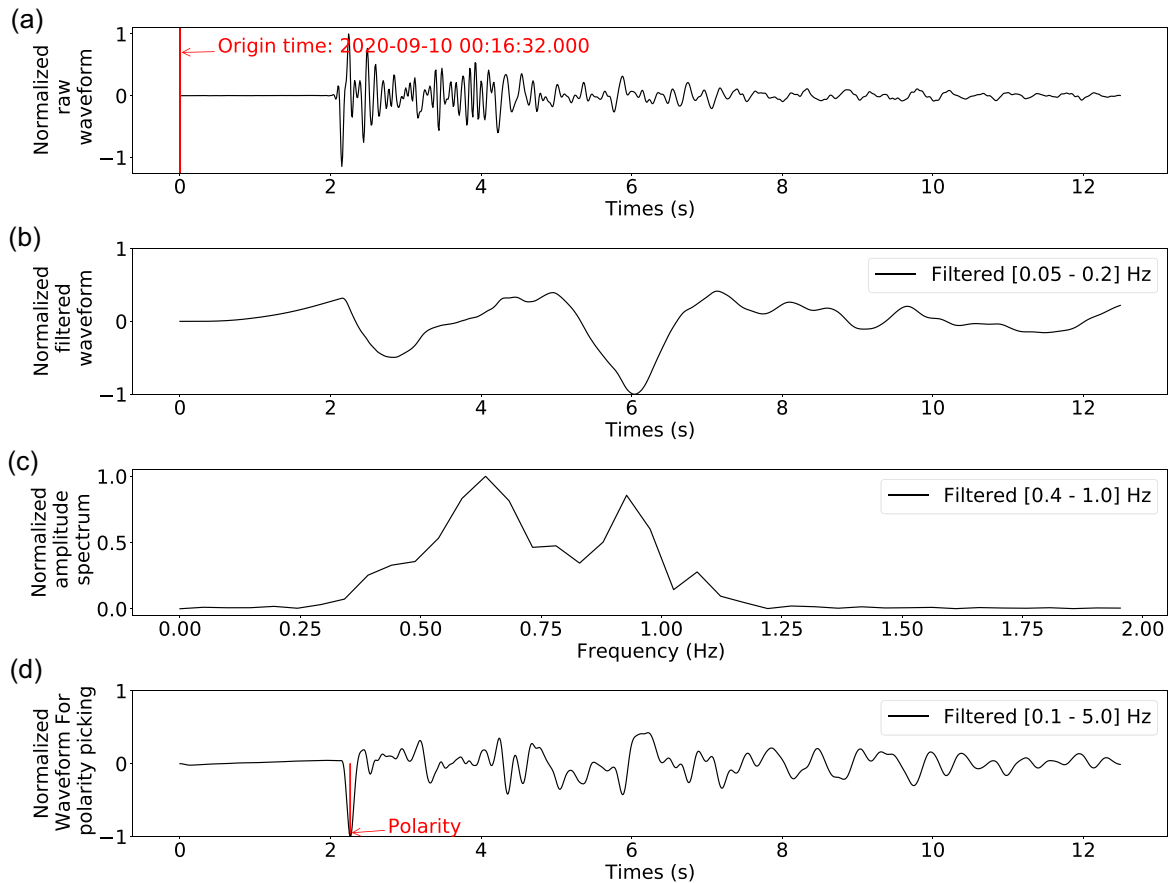


**Figure 1.** An example of data sets: (a) The vertical component recording at station BCH2A for the  $M_L$  2.5 10 September 2020, event at 6-km epicentral distance and  $15^\circ$  azimuth. The origin time in local time (red) is also shown. (b) Waveform of (a) filtered between 0.05 and 0.2 Hz. (c) Amplitude spectrum of (a) filtered between 0.4 and 1.0 Hz. (d) Waveform of (a) filtered between 0.1 and 5.0 Hz for polarity picking.  $P$ -wave first motion polarity pick is shown (red).

## 2.2 Joint inversion of multiple seismic data types

In this work, we consider multiple seismic data sets extracted from the raw waveforms at various frequency bands. These include long-period waveforms, spectra and polarities. Therefore, the data vector is a concatenation of three data types  $\mathbf{d} = [\mathbf{d}^w, \mathbf{d}^s, \mathbf{d}^p]$ , where  $w$ ,  $s$  and  $p$  represent waveforms, spectra and polarities, respectively. The likelihood function for all data is based on the assumption that the noise on each type of data is independent of that on other data types. Therefore, the total likelihood is the product of the individual data types

$$L(\mathbf{m}) = L_w(\mathbf{m})L_s(\mathbf{m})L_p(\mathbf{m}). \quad (2)$$

The assumption of independent noise requires care in selecting spectra and waveforms when applying this method. To ensure that noise between data types is reasonably independent, we only apply non-overlapping frequency bands.

The polarity likelihood function attributes higher probability to rays that have a greater theoretical amplitude (Brillinger *et al.* 1980). The polarity likelihood function is given by

$$L_p(\mathbf{m}) = \prod_{i=1}^N \pi_i^{\frac{(1+d_i^p)}{2}} (1 - \pi_i)^{\frac{(1-d_i^p)}{2}}, \quad (3)$$

where  $N$  is the number of the observed polarity data, and  $\mathbf{d}_i^p$  denote the observed polarity at station  $i$ . The function  $\pi_i$  is given by

$$\pi_i = \gamma + (1 - 2\gamma)\Phi\left(\frac{A_i(\mathbf{m})}{\sigma}\right), \quad (4)$$

where the cumulative distribution function (CDF) of the normal distribution,  $\Phi$ , estimates the probability of first motions based on its theoretical amplitude  $A_i(\mathbf{m})$  calculated by a seismic source ( $\mathbf{m}$ ) (Aki & Richards 2002). To quantify the uncertainty, we follow Brillinger *et al.* (1980) and consider  $\sigma$  as the standard deviation of modelling errors ( $\sigma > 0$ ). The parameter  $\gamma$  ( $0 \leq \gamma \leq 0.5$ ) defines the probability that the polarity has been picked incorrectly. However, for high signal-to-noise ratio (SNR) data,  $\gamma$  may be considered small. Positive and negative polarities at stations are considered to be  $\pm 1$  for first motions.

To formulate a likelihood function for waveform and spectrum data, we assume Gaussian-distributed noise on waveform data. However, it is important to note that amplitude spectra are intrinsically positive and are derived from filtered waveforms. Therefore, if waveforms are contaminated by Gaussian-distributed noise, the noise on amplitude spectra is Rice-distributed (Rice 1944). In the case of SNR values that we expect for this application, the Rice distribution is well approximated by a Gaussian distribution (Yakovleva 2019). Therefore, a multivariate Gaussian distribution with an unknown standard deviation is assumed for waveform and amplitude spectrum data. In this case, the likelihood function for  $K_I$  channels,

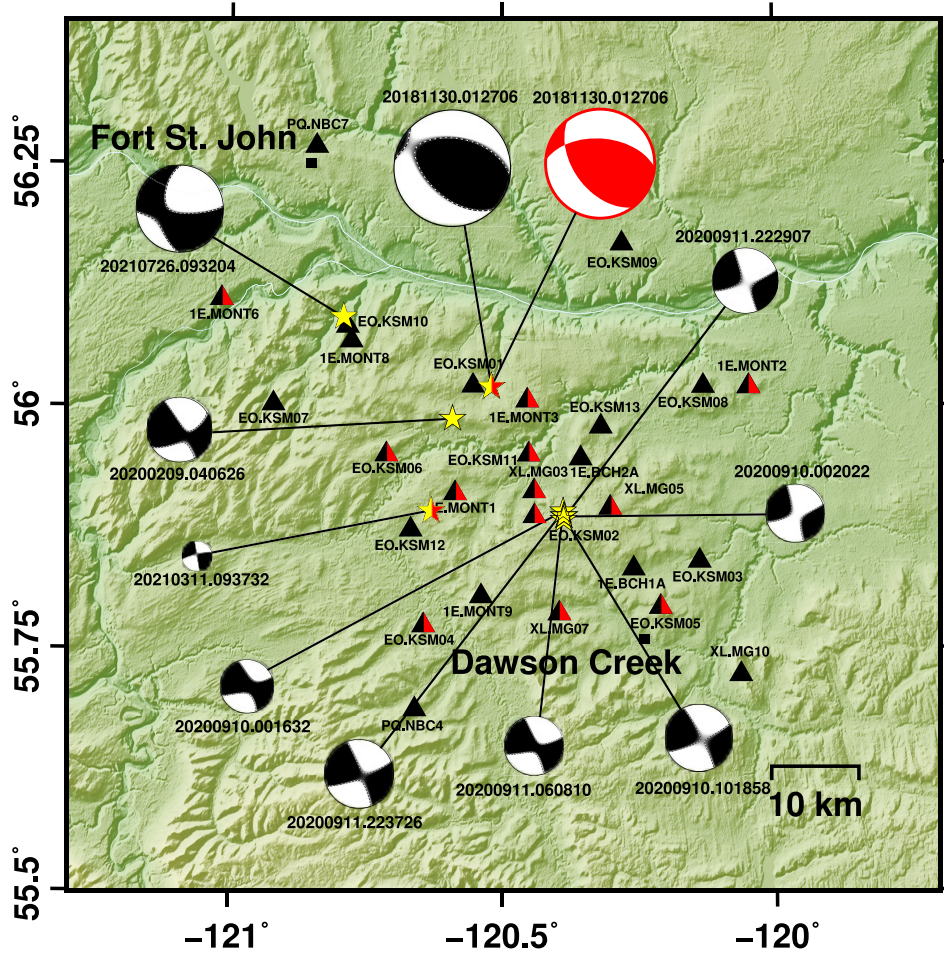


**Figure 2.** Map of the study region with centroid moment tensor results. Event locations (yellow stars) are shown for each solution, sizes of focal mechanisms are scaled by magnitudes, the fuzziness of the focal mechanism represents uncertainty and mechanisms are labelled with inferred origin times. The red focal mechanism refers to the solution obtained by Peña Castro *et al.* (2020). Stations that recorded real data for source inference are shown as black triangles. Two-coloured triangles and stars show stations and events that are considered for simulations. Black squares are settlements in the area.

**Table 1.** Case descriptions. Rows explain the data type of each station and frequency bands used in the inversion.

Case	Data		
	Waveform	Spectrum	Polarity
1	KSM04 [0.05–0.2] Hz		
2	KSM04 [0.05–0.2] Hz		39
3		KSM04 [0.3–3.3] Hz	39
4	KSM04 [0.05–0.2] Hz	KSM{02,04,05,06,11},MG07 [0.3–1.0] Hz	39
5	KSM04 [0.05–0.2] Hz	KSM{02,04,05,06,11},MG07 [2.3–3.0] Hz	39

where  $l \in [w, s]$  represents the type of data (waveforms or spectra), is given by

$$L_l(\mathbf{m}) = \prod_{k=1}^K (2\pi)^{-N_k^l/2} |\mathbf{C}_k|^{-1/2} \exp\left[-\frac{1}{2}(\mathbf{d}_k^l - \mathbf{d}_k^l(\mathbf{m}))^T \mathbf{C}_k^{-1} (\mathbf{d}_k^l - \mathbf{d}_k^l(\mathbf{m}))\right]. \quad (5)$$

Here,  $\mathbf{d}_k^l(\mathbf{m})$  are predicted data for model  $\mathbf{m}$ ,  $\mathbf{d}_k^l$  are observed data,  $\mathbf{C}_k^l$  are covariance matrices and  $N_k^l$  are the number of data. Note that the  $K_l$  data vectors are concatenated in  $\mathbf{d}^l$ .

### 2.3 Covariance estimation for joint inversion

Uncertainty quantification (UQ) is required for meaningful interpretation of results (Jaynes 2003). For geophysical inference, UQ should be based on measurement errors and theory errors (Tarantola & Valette 1982). Measurement errors are attributed to noise during measurement, and theory errors arise from assumptions in the mathematical formulation and parametrization. In the formulation of the likelihood function, both types of errors can be considered by iterative estimation of covariance matrices based on residual errors (Dettmer *et al.* 2007). In this approach, non-Toeplitz covariance matrices,  $\mathbf{C}_k$ , are estimated from the autocovariance function of the residuals. An initial estimate of  $\mathbf{m}$  is needed to calculate the residual between observed and predicted data, and we use the solution as obtained by Bayesian inference assuming uncorrelated noise.

This covariance parametrization accounts for theory errors such as, for example centroid location and velocity model mismatch (Vasyura-Bathke *et al.* 2021). Therefore, the likelihood function is not biased by assuming uncorrelated errors when long-period noise is present in waveforms that are sampled at high rates. In joint Bayesian inference, the noise treatment and the number of data samples can affect the weight of a data set such that waveforms or spectra can dominate the joint inversion without proper weighting factors. Consequently, it is crucial for joint inversion to avoid

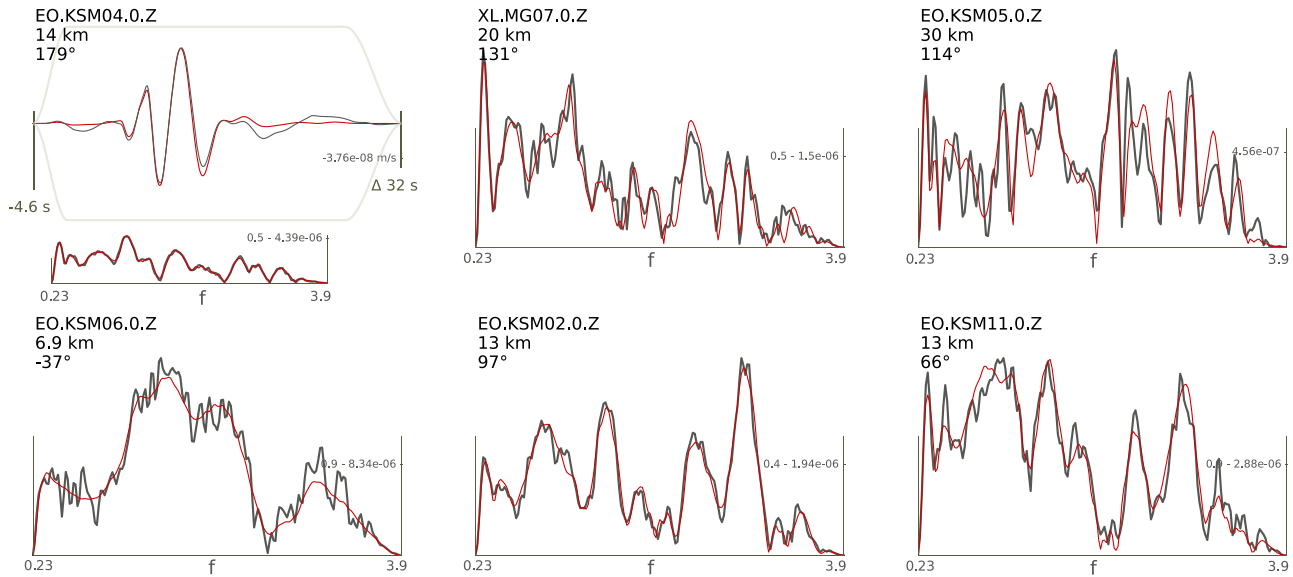


**Figure 3.** Noise-free (red) and noisy (grey) simulated data. Examples for one channel with waveform and spectrum (top left), and five channels with only spectra, are shown. Station code, channel, epicentral distance and azimuth are shown in the top left of each panel. Maximum amplitude and frequency bands for spectra are shown in the top-right corner and on the horizontal axis, respectively. The waveform and spectra are filtered between 0.05–0.2 and 0.3–3.3 Hz, respectively.

assigning unreasonably high likelihood values to waveforms with high sampling rates. In addition, choosing a time window that does not contain constraining information may increase only variance reductions with ineffective number of samples. Hence, sampling rate and window length should be chosen with care. Furthermore, in hierarchical Bayesian inference, noise scaling factors are considered as unknown parameters. These scaling parameters can erroneously reduce data set weights. Empirically, the non-Toeplitz covariance matrix lowers the chance of estimating incorrect noise scalings (Vasyura-Bathke *et al.* 2021).

## 2.4 Data predictions

To produce multi-component waveforms for an MT source, we assume a 1-D Earth structure with homogeneous layers described by thickness, density, seismic-wave velocity and attenuation. Green's functions, composed of a linear combination of ten (eight for the far field) elementary seismograms, are computed for an appropriate source–receiver volume to predict 10-Hz waveforms for a general moment tensor source (Wang 1999; Heimann 2011; Heimann *et al.* 2019). Amplitude spectra are produced by taking the square root of the sum of squared real and imaginary parts of the Fourier transform of waveforms. In addition, we calculate the radiation pattern for  $P$  waves using

$$R^P = \Gamma^T \mathbf{M} \Gamma, \quad (6)$$

where  $\mathbf{M}$  is the moment tensor in northeast-down coordinates, and  $\Gamma$  are coefficients for a station with specific epicentral distance and azimuth

$$\Gamma = \begin{pmatrix} \sin \theta \cos \phi \\ \sin \theta \sin \phi \\ \cos \theta \end{pmatrix}, \quad (7)$$

where  $\theta$  are take-off angles that can be computed from the Earth structure, epicentral distances and depth of the events and  $\phi$  are azimuths of the receivers. These coefficients describe the amplitude of the different components at the source. The displacement

components are given by (Aki & Richards 2002; Pugh *et al.* 2016)

$$u^P = \frac{1}{4\pi\rho\alpha^3r} (\Gamma^T \mathbf{M} \Gamma) \Gamma = F_P (\Gamma^T \mathbf{M} \Gamma) \Gamma, \quad (8)$$

where  $F_P$  is the propagation effect, including geometrical spreading and the effects of the Earth structure that we defined before.

We estimate the PPD numerically with a sequential Monte Carlo sampler (e.g. Del Moral *et al.* 2006; Vasyura-Bathke *et al.* 2020). Samples are independent and based on a sequence of intermediate, annealed bridging distributions from the prior to the posterior. An annealing parameter enables the transitioning between distributions by scaling from the prior to the posterior. In this algorithm, samples can initially move freely in the parameter space but gradually become more constrained by the data as the sample approaches the posterior.

## 3 STUDY AREA AND DATA

Since the main focus of this work is inversion for small earthquakes ( $M < 4$ ), often only few impulsive, high SNR waveforms are available. The typically most reliable long-period signals (0.01–0.2 Hz) of such events can be weak and of poor SNR. The intermediate periods (0.2–2.0 Hz) are often complicated by coda with several interfering phases. However, complexity can be reduced significantly by removing phase information in the spectral domain. By only considering the amplitude information of the spectrum, predictions are more straightforward and can be successfully carried out at intermediate frequencies. This permits exploiting higher frequencies up to 2 Hz in the source inversion.

Similarly, first motion polarities are picked on broad-band waveforms, which contain information that is removed by filters in the case of waveforms or spectra. Since only the sign of the arrival is retained and since station coverage is usually sparse, polarities allow resolving mostly the double-couple (DC) MT component. However, constraining these via polarities reduces parameter uncertainties for other parameters of the CMT, which in turn can be constrained by

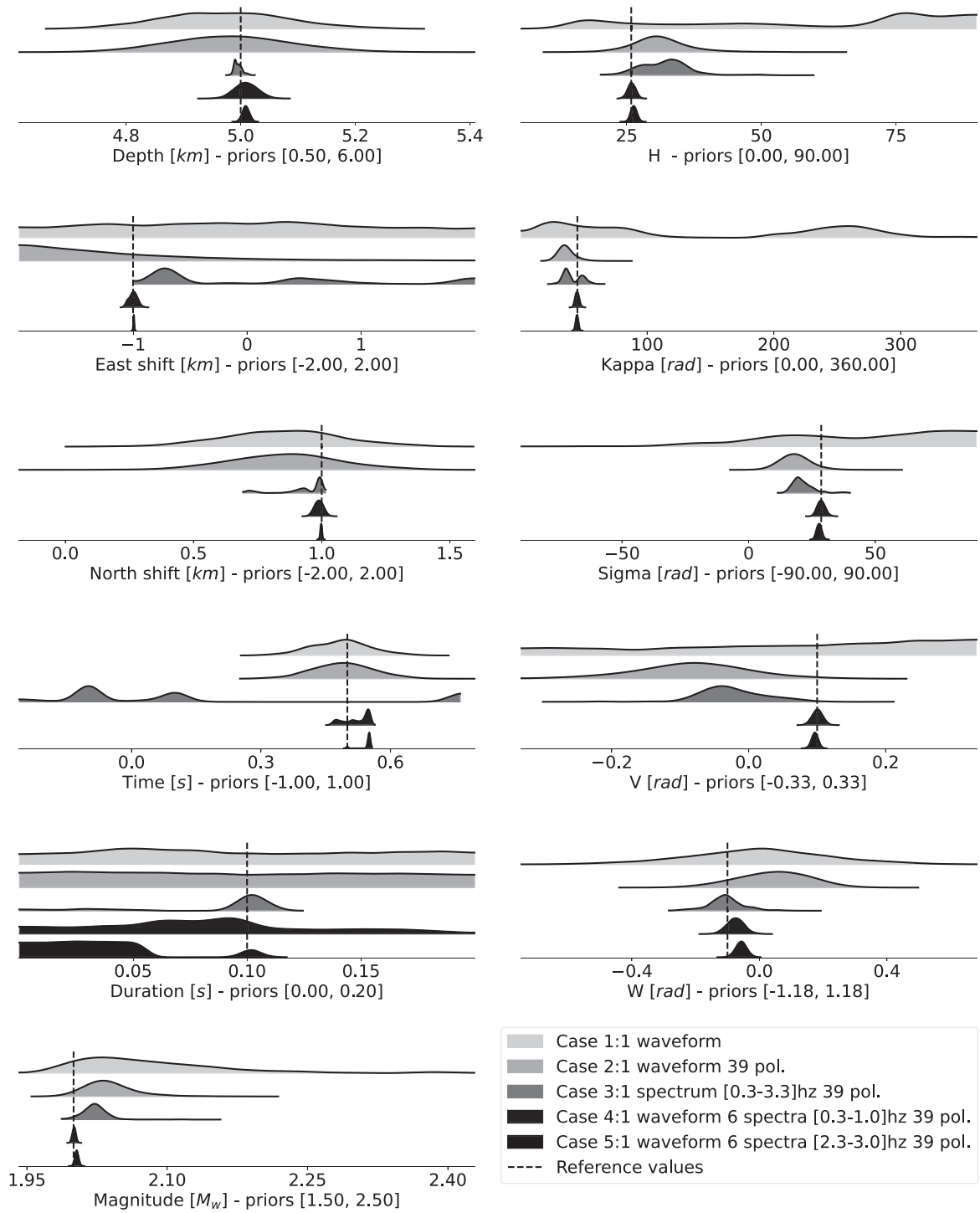


**Figure 4.** Marginal posterior distributions of the solutions obtained for simulation cases 1–5. Each panel shows cases from 1 to 5 from top to bottom rows, respectively. When only four rows are shown, the particular parameter is not part of the parametrization for that case. Dashed lines represent true values. Each panel is labelled with parameter name and the prior bounds.

the other data types. Polarities are the simplest seismic data and straightforward to predict. Here, we extract long-period waveforms from 0.05 to 0.2 Hz, amplitude spectra from 0.3 to 1.2 Hz, and polarities from the broad-band waveforms.

We consider data from various networks in the Kiskatinaw Seismic Monitoring and Mitigation Area (KSMMA) in northeastern

British Columbia, Canada. Data are accessed via IRIS and include permanent and temporary stations. Most stations are obtained from the McGill University and University of Calgary networks. The station coverage in the  $50 \times 50$  km area is high with an average station spacing of 20 km (Fig. 2). We consider data recorded between January 2020 and February 2022 (Salvage *et al.* 2021). Seismic events

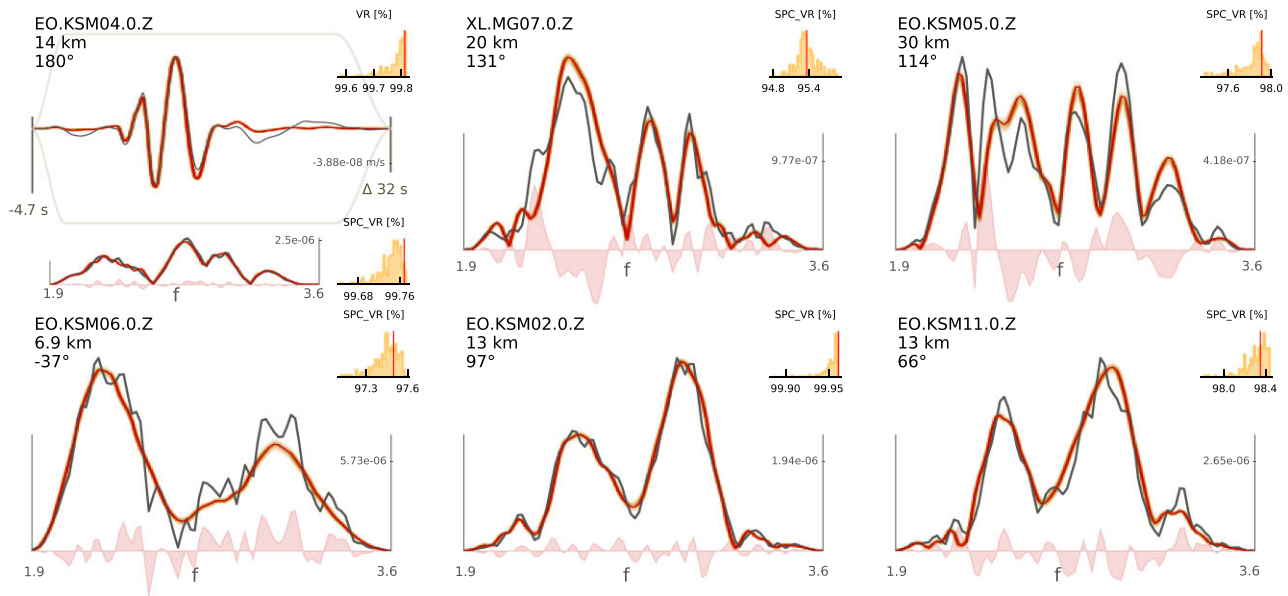


**Figure 5.** Data fits for case 5: Simulated waveforms and amplitude spectra (grey); maximum *a posteriori* (MAP) predictions (red) and spectra residuals (shaded polygons) are shown. The brown shading is for 200 randomly selected samples from the posterior predictive distribution. Panels are annotated with station code, component, epicentral distance and azimuth obtained for the MAP solution. The arrival time with respect to the centroid time, and the length of each window are shown in the lower-left and lower-right corners, respectively. The weighted variance reductions for the posterior predictive distribution are shown in the top-right corners. The waveform and spectra are filtered between 0.05–0.2 and 2.3–3.0 Hz, respectively.

**Table 2.** Descriptions of the illustrative cases applied to the  $M_w$  4.2 30 November 2018, event. For further details, see Table 1.

Case	Data		
	Waveform	Spectrum	Polarity
1	MONT3 [0.03–0.12] Hz		
2	MONT3 [0.03–0.12] Hz		36
3		MONT3 [0.12–0.5] Hz	36
4	MONT3 [0.03–0.12] Hz	MONT{1,2,3,6},MG0{3,5} [0.12–0.5] Hz	36
5	40 waveforms [0.03–0.07] Hz		

used in this study are associated with hydraulic fracturing operations, and are expected to be small and shallow. The largest event of 30 November 2018, of  $M_w$  4.2 produced 40 high-quality waveform recordings. The smallest one of 11 March 2021, of  $M_L$  1.6, produced only one usable waveform. This region is known for having induced earthquakes due to multistage hydraulic fracturing injections, and has received significant attention (e.g. Mahani *et al.* 2017, 2020; Fox & Watson 2019; Peña Castro *et al.* 2020; Salvage *et al.* 2021; Salvage & Eaton 2022). Many previous events were found to be dominantly strike slip. However, complex flower structures can cause earthquakes with a variety of mechanisms in a small region (e.g. Barclay *et al.* 1990; Mei 2009; Wozniakowska *et al.* 2021).

## 4 RESULTS

### 4.1 Simulation examples

In this section, we present the results of five different simulation examples, that is ‘cases’ in the following, to evaluate the validity of the method. In these cases, we use varying combinations of simulated data to test the influence of each data type on the ability to constrain CMT parameters. These cases are summarized in Table 1.

An oblique CMT with moment magnitude 2.0 is considered to produce waveform data in units of velocity with a sampling rate of 10 Hz and 39 polarities. Synthetic data are contaminated by filtered Gaussian noise to mimic the SNR of waveforms recorded for an  $M_L$  1.6 event in the region. A 20-s signal window around the *P*-wave arrival and a 20-s noise window before the *P* wave are considered to measure the SNR on filtered field data. All data are chosen based on their long-period SNR (Fig. 3). In addition, theoretical amplitudes are contaminated by 10 per cent Gaussian noise to produce noisy polarity data. The noise scaling factor for polarity is considered to be a hierarchical parameter with a prior between 0.0 and 0.2. Furthermore, the noise on waveforms and spectra is estimated as a non-Toeplitz covariance matrix (Dettmer *et al.* 2007).

For case 1, we consider only the waveform of KSM04 shown in Fig. 3 to constrain the parameters of the CMT. The data are bandpass filtered between 0.05 and 0.2 Hz and cosine-tapered with a 32-s time window around the *P*-wave arrival. For case 2, we add *P* wave first motion polarities to the data of case 1. For case 3, the waveform of KSM04 is transformed to the spectral domain. We consider a 26-s time window around the *P*-wave arrival prior to the Fourier transform and we filter the spectrum to 0.3–3.3 Hz. Cases 4 and 5 include one waveform, 6 spectra and polarities. The difference between these two cases is the frequency band for the amplitude spectra. We filter amplitude spectra between 0.3–1.0 Hz and 2.3–3.0 Hz for cases 4 and 5, respectively.

PPDs and waveform/spectra/polarity-fits for all cases are summarized in Figs 4 and S1–S6, respectively. By comparing histograms of first and second cases in each panel, we observe that the added polarity data in case 2 contribute significantly in reducing parameter uncertainties and, in particular, better constraining the source focal mechanism parameters, that is *H* (dip), *Kappa* (strike) and *Sigma* (rake). A comparison of the second and third cases shows that replacing waveforms with spectra in the joint inversion resolves most parameters similarly well, such as DC source parameters. Although the model parameters depth and magnitude are notably better re-

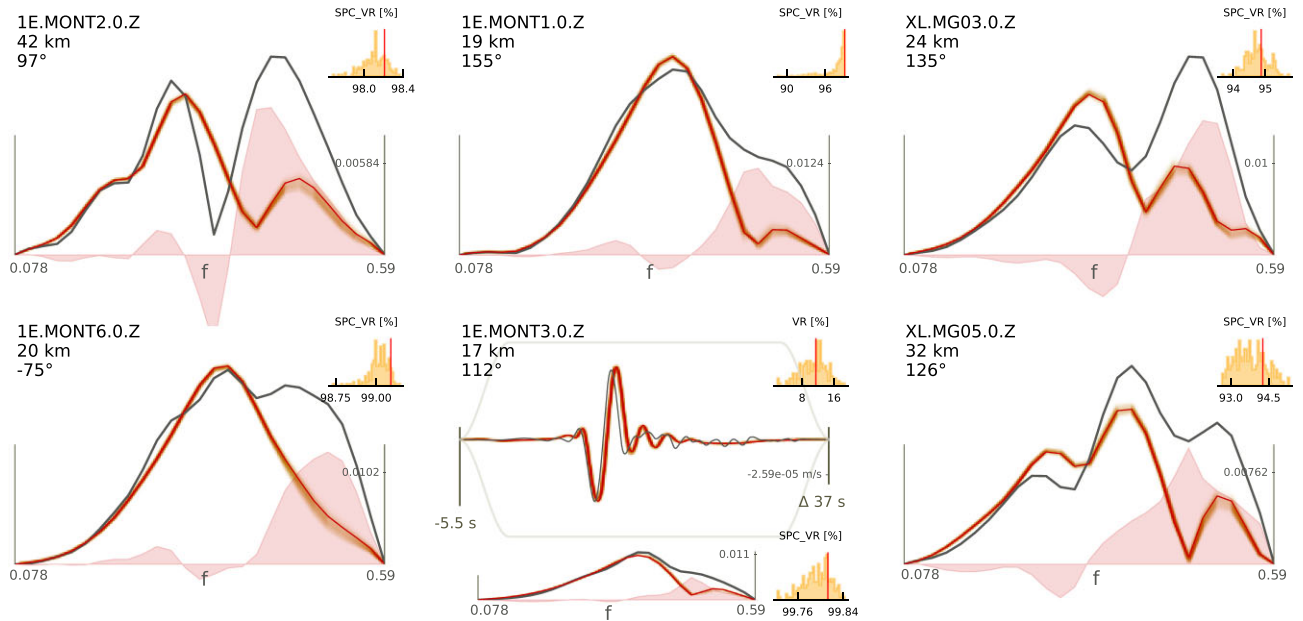


**Figure 6.** Spectrum and waveform fits for CMT inversion of the  $M_w$  4.2 30 November 2018, event. The waveform and spectra are filtered between 0.03–0.12 and 0.12–0.5 Hz, respectively. For further details, see Fig. 5.

solved, the spectrum, the location shift parameters and centroid time are less well constrained in case 3 due to the discarded phase spectra information.

Cases 4 and 5 consider joint inversion with two different frequency bands to illustrate the influence of intermediate-frequency data, that is spectra, in joint inversion. Data fits for the fifth case are plotted in Fig. 5 and show that the inversion is able to fit the main phase with high variance reduction. Posterior distributions (Fig. 4) indicate that CMT parameters are well resolved by each of these last two cases. A comparison between the posterior distributions of these cases demonstrates that uncertainties of centroid and lune parameters decrease significantly when data of higher frequency range are included in the inversion. In the amplitude spectra inversion, discarding phase information causes errors in arrival times. Consequently, solutions obtained from inversions with spectra-only data are highly ambiguous. The estimated covariance matrices for waveform and spectrum at station KSM04 for case 5 show highly correlated noise and uncorrelated noise, respectively (Fig. S7).

## 4.2 Field data examples

### 4.2.1 The $M_w$ 4.2 Fort St John earthquake

In this section, we apply five cases to the  $M_w$  4.2 30 November 2018, event (Table 2), and vary combinations of data types to consider their ability to constrain CMT parameters. We chose this event because it has many high-quality waveforms to consider as the basis for a reference solution. The MAP solution that we obtain for this event using 40 waveforms is consistent with previous studies (e.g. Peña Castro *et al.* 2020) and we refer to it as the ‘reference solution’ in the following (Fig. 7).

Seismic waveform data are restituted, downsampled to 10 Hz, and rotated to source–receiver geometry to obtain high SNRs on horizontal components. A 0.03–0.12 Hz bandpass filter is applied

to the 37-s time window around the  $P$ -wave arrival on the waveform while amplitude spectra for 26-s windows are fit between 0.12 and 0.5 Hz. We picked 36 polarities for the most impulsive waveforms.

Data that are included in cases 1 through 5, respectively, are a single waveform; single waveform and 36 polarities; single spectrum and 36 polarities; single waveform, 6 spectra and 36 polarities and 40 waveforms (Table 2). The waveform and spectra for station MONT3 are chosen for the field data cases 1 through 3 since it is the closest station with the highest SNR. The best solution was obtained in case 4 and not only does it fit the main phase of the waveform well, but it also matches the amplitude spectra for the lower frequency band, where events with such a magnitude excite strong long-period signals (Fig. 6).

Posterior marginal distributions of the solutions estimated for the five cases and the waveform inversion are summarized in Fig. 7. Comparing cases 1 and 2 demonstrates that polarity data contribute significantly to resolving the focal mechanism. Comparing cases 3 and 4 shows that incorporating intermediate frequencies reduces uncertainty of some parameters such as depth and magnitude. Although most parameters are resolved similarly to case 2, other parameters such as time and location shifts are less well resolved. Finally, comparing the results of the joint inference from case 4 with case 5 shows that all parameters have similar MAP solutions, with small uncertainties although they are somewhat larger in case 4 than for case 5. Nonetheless, we conclude that the solution obtained by the joint data set inversion (case 4) is of comparable quality to the reference 40-waveform inversion (case 5). Notably, the lune parameters of the moment tensor obtained by the joint inversion indicate a nearly pure DC moment tensor. This result is also illustrated by the MT decomposition (Fig. 8). This is reassuring, since high non-DC components for earthquakes may indicate susceptibility to theory errors. In fact, such non-DC components are often the reason to constrain the MT to special cases (Vasyura-Bathke *et al.* 2021).

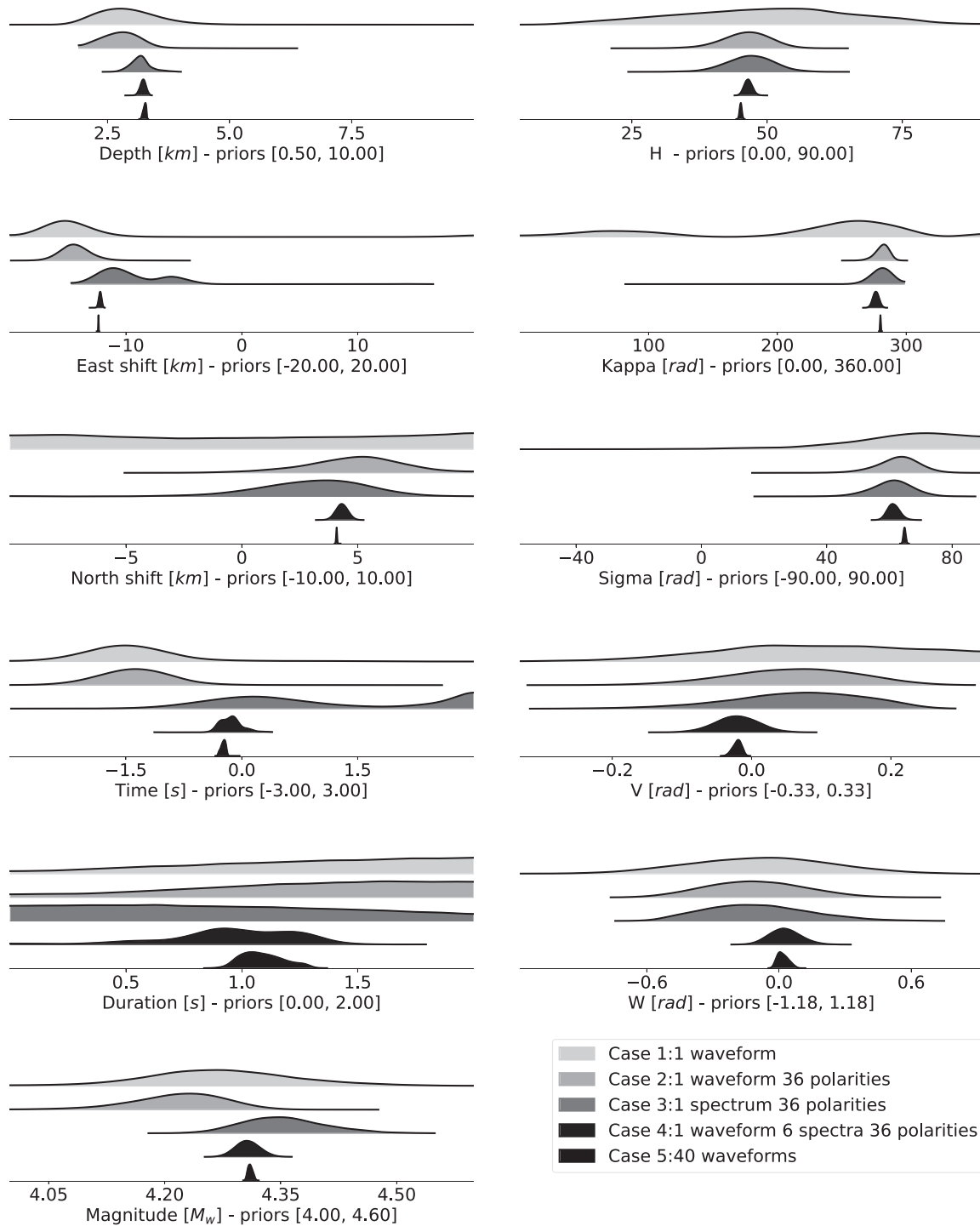


**Figure 7.** Posterior distributions of the solutions of the  $M_w$  4.2 30 November 2018 event obtained by waveform and joint inversions. For further details, see Fig. 4.

#### 4.2.2 Ten $M_w \leq 3$ local/regional events

Finally, we jointly invert the available data of 10 events. For  $M \leq 3$  events, Bayesian waveform inversion often is barely able to resolve source parameters due to limited data quality. Therefore, we incorporate fewer but high-quality waveforms in our inversions. As a representative example, CMT results for the  $M_L$  2.5 10 September 2020, event are discussed here in detail. This event has one

high-quality waveform, along with a number of acceptable spectra (Fig. 9). We use data from stations at epicentral distances up to 50 km. A 30-s and 23-s window around manually picked body wave arrivals is considered for the single waveform and amplitude spectra, respectively. A third-order bandpass filter between 0.05 and 0.2 Hz is applied to the waveform, and a frequency filter between 0.4 and 1.0 Hz is applied to spectra. In addition, polarities are picked

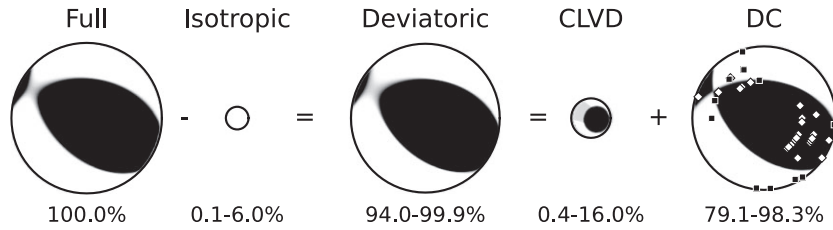


**Figure 8.** Moment tensor decomposition and polarity fit of the solutions for the  $M_w$  4.2 Fort St John event (30 November 2018) obtained by the joint inversions of one waveform, 6 spectra and 36 polarities (case 4). White diamonds and black squares show positive and negative polarities.

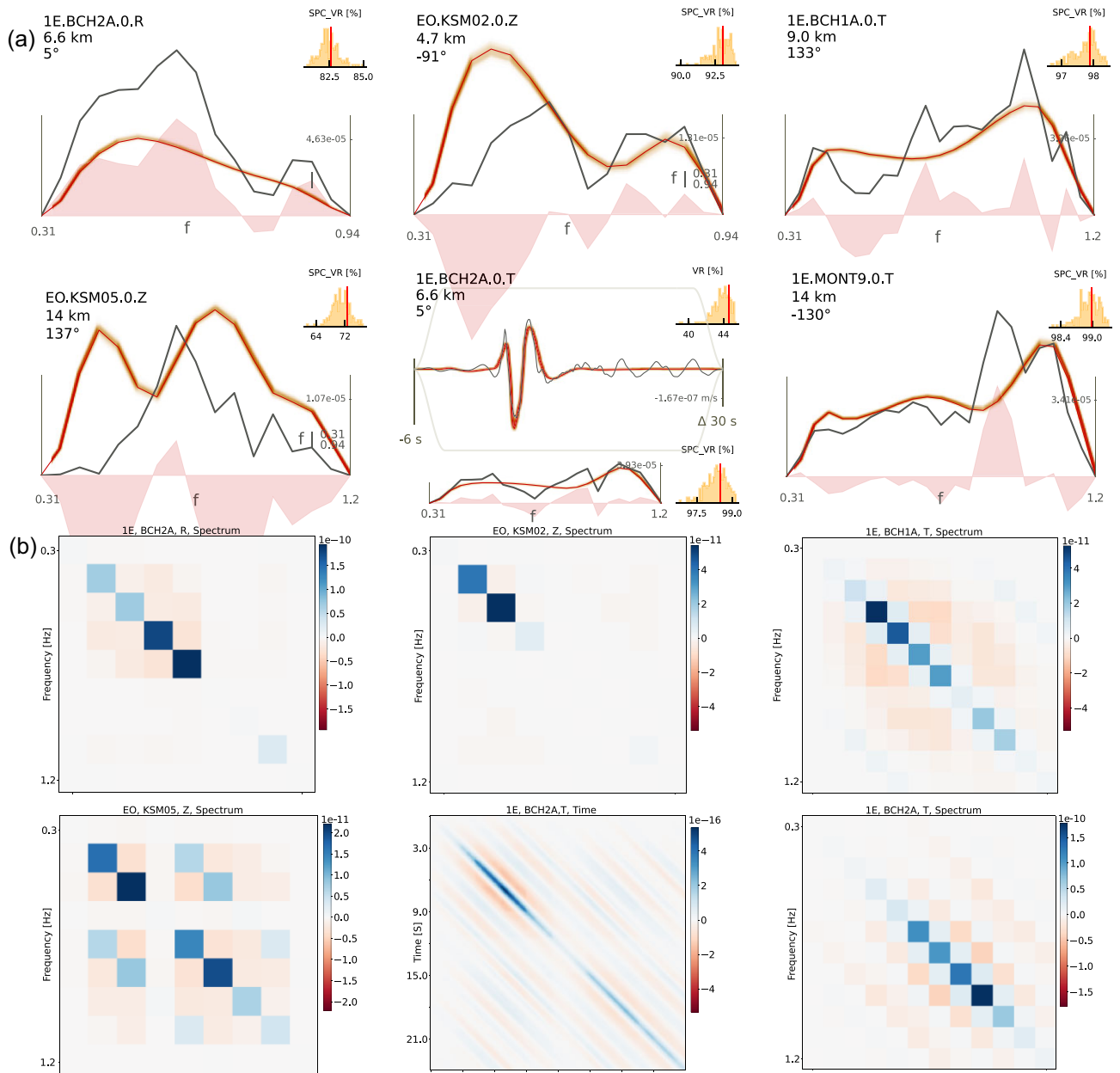


**Figure 9.** (a) Spectrum and waveform fits and (b) covariance matrices of residuals for the CMT inversion of  $M_L$  2.5, 10 September 2020, event. The waveform and spectra are filtered between 0.05–0.2 and 0.4–1.0 Hz, respectively. The two last rows show non-Toeplitz covariance matrices estimated on the residuals of the MAP solution. For further details, see Fig. 6.

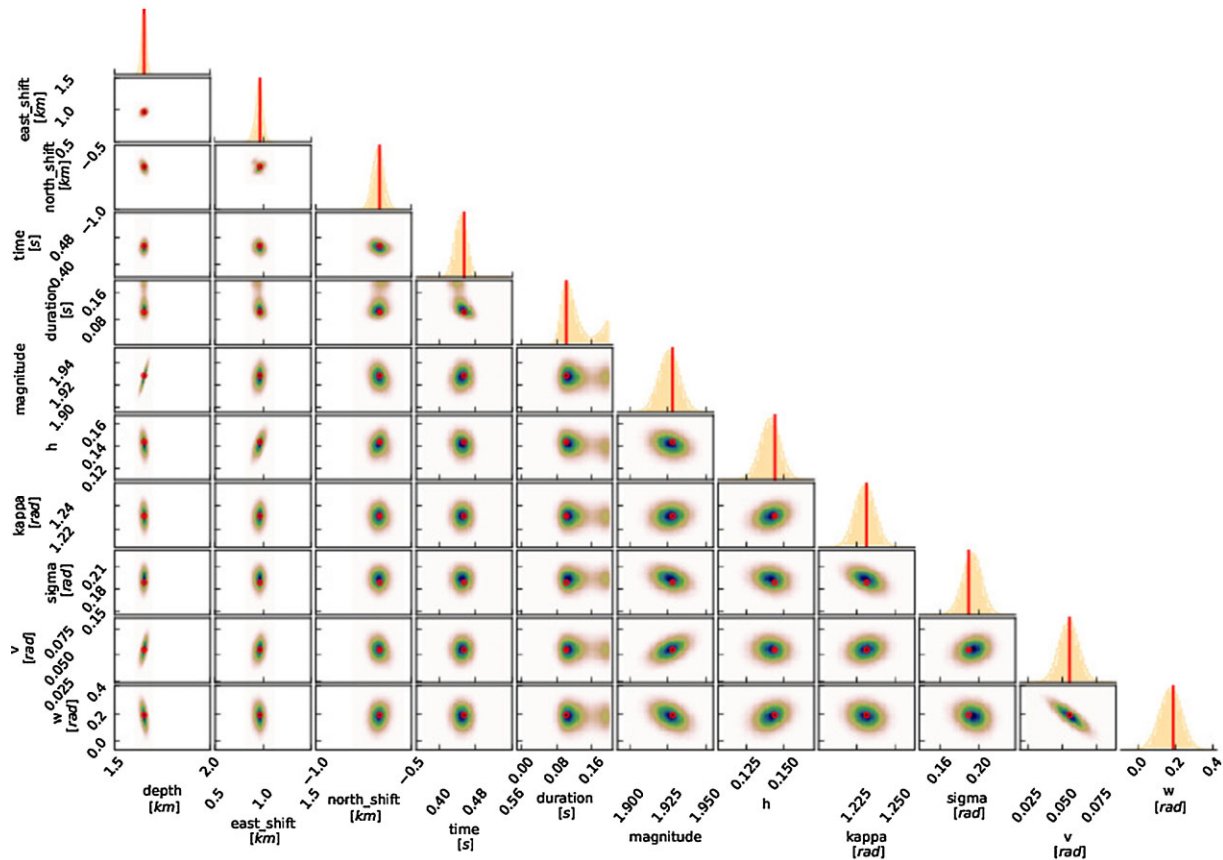


**Figure 10.** Posterior distributions of the solutions of  $M_L$  2.5 10 September 2020, event obtained by joint inversion. Red lines show MAP model parameters.

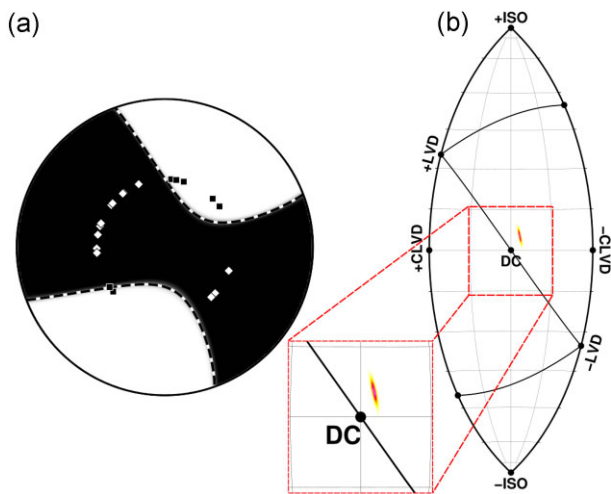


**Figure 11.** (a) Fuzzy focal mechanism with polarity fit and (b) lune of the solution obtained for  $M_L$  2.5 10 September 2020 event.

manually on displacement data that are filtered in the frequency band of 0.1–5.0 Hz.

The results are presented as an example of waveform fits, which include 200 random samples of the ensemble, and covariance matrices (Fig. 9); 2-D posterior distributions (Fig. 10) that show qualitative statistics of model parameters and their correlations; the fuzzy focal mechanism and the lune (Fig. 11) that illustrates marginalization for the moment tensor decomposition. Dependability of the solutions are evaluated by data fits (Fig. 9), such that waveform

fits are demonstrated in terms of the posterior predictive distribution and fits on waveform and spectra are quantified by variance reduction (Vasyura-Bathke *et al.* 2020). The majority of predictions fit the main trend of the waveform and amplitude spectra. In addition, the inversion successfully resolves the amplitude of the waveform and those of amplitude spectra, which raises confidence that the depth and magnitude are well estimated. Generally, transverse signal components are better explained than others due to less complexity. Examples of the estimated non-Toeplitz covariance matrices for waveform and spectra at different stations for this event show correlation highlighting the importance of including correlated noise components in the noise estimation (Fig. 9).

CMT parameters are resolved with low uncertainty and modes of the distribution are generally near the MAP model (Fig. 10). The strongest correlations can be observed between the longitude ( $v$ ) and latitude ( $w$ ) of the lune parametrization, and magnitude and depth of the event. Among centroid parameters, only east shift has a mild correlation with dip ( $h$ ). The estimated depth and magnitude of the MAP model are the same as their corresponding catalogue values. Centroid location shifts are reasonable and small, which means that the catalogue location was reasonable. At  $\sim 0.1$  s, the STF length (duration) is also reasonable for this magnitude. Fault geometry parameters indicate a strike-slip mechanism caused by the NW–SE or SW–NE movement on a nearly vertical fault surface.

The fuzzy focal mechanism for the solution (Fig. 11) shows a strike-slip mechanism with well-fit polarity data. Parameters  $V$  and  $W$  of the lune parametrization (Fig. 10) refer to deviatoric and isotropic components of the source mechanism, respectively. Here, these parameters are small, which suggest that the source mechanism is nearly a pure DC. In addition, the lune plot (Fig. 11)

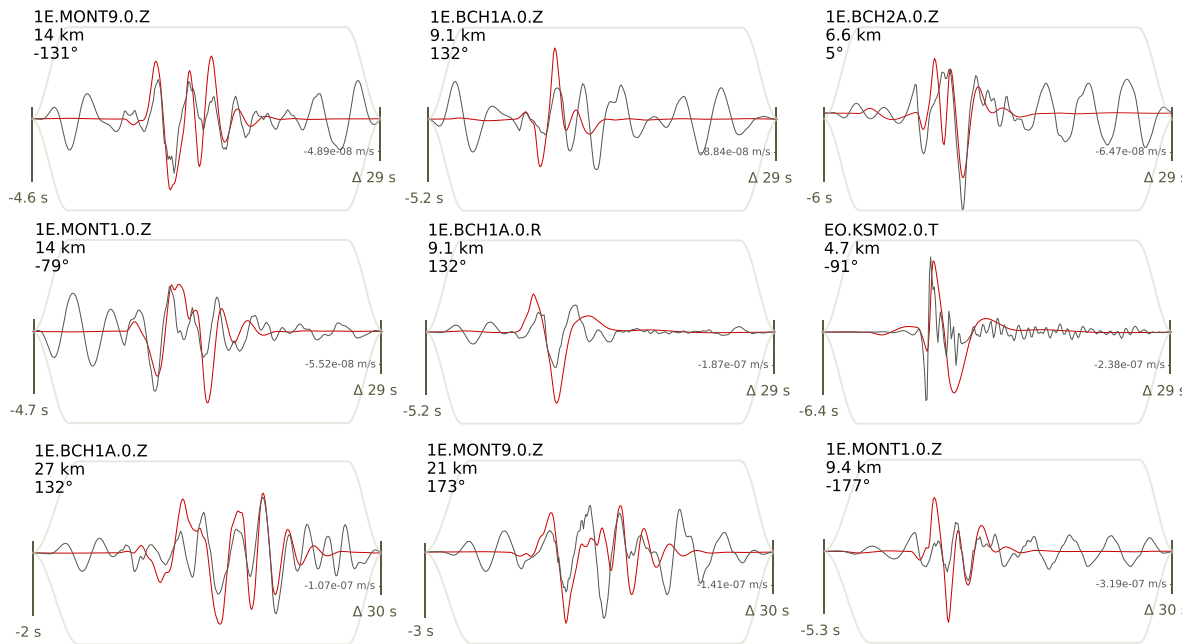


**Figure 12.** Examples of agreement between noisy waveforms not included in the inversion and prediction generated with the MAP model for these locations. The predicted waveforms agree with main data features, indicating a robust result.

presents the same information as a 2-D marginal. Although not concerning, the small non-DC component is expected for induced events, but still could be an artefact of the inference (e.g. Valentine & Woodhouse 2010; Vasyura-Bathke *et al.* 2021).

To summarize the results for all events, we present a map of fuzzy focal mechanisms obtained by the joint inversion (Fig. 2). Most mechanisms are strike-slip dominated, while some include oblique thrust.

To further study the quality of the CMT solutions, we present comparisons of observed waveforms with predicted waveforms for channels not included in the inversion. Fig. 12 shows that the solutions of two events match the main phase even for waveforms with poor SNR (e.g. MONT01, BCH1A, BCH2A and MONT09). This also supports the claim that we are able to resolve CMT models with a small number of stations with little azimuthal coverage. However, this result depends on the station setting and also path effects. Thus, a higher azimuthal station coverage is usually desirable.

## 5 DISCUSSION AND CONCLUSION

We applied Bayesian joint inversion of waveforms, spectra and polarities with noise covariance estimation to several earthquakes of  $M < 3$ . Source inversions may suffer from a lack of high-quality data for small to moderate earthquakes due to weak long-period excitation and/or sparse station coverage. In addition, the solution obtained by including highly contaminated waveform data may be unreliable. We choose only a single or few high-quality waveforms and exclude those that are noisy or produce poor variance reductions. Since these few waveforms are insufficient to resolve CMTs with low uncertainty, the information is complemented by amplitude spectra and first-motion polarities. All data are extracted from seismic waveforms but in distinct frequency bands: Polarity data are picked on broad-band waveforms filtered

between 0.1 and 5.0 Hz, amplitude spectra are in the intermediate band from 0.3 to 1.2 Hz, and waveforms are in the band 0.05–0.2 Hz.

We apply Bayesian inference to our joint inversion to quantify the uncertainties of model parameters. In this framework, we consider two likelihood functions based on the assumption of Gaussian-distributed noise on the raw waveform data. Since the number of data vary significantly for the three data types, it is crucial to account for data covariances in the case of spectra and waveforms. Otherwise, polarity data would be overwhelmed by the other two data types or require subjective weighting. Covariance estimation is by an iterative method, performed during early stages of sampling and produces a non-Toeplitz covariance matrix (Vasyura-Bathke *et al.* 2021). Inclusion of these covariance matrices removes the requirement for subjective data weights from the joint inversion. Further, the non-Toeplitz covariance matrix also accounts for velocity model mismatch, centroid location errors and other theory errors intrinsically.

An assumption in the likelihood function (eq. 2) is the independence of noise: The formulation assumes that the noise of a particular data type is not correlated with the noise on the other data types. The justification for this formulation is that the waveforms and spectra are processed for non-overlapping frequency bands. To support this assumption, we considered pre-earthquake noise, processed identically to data employed in the inversion. For each event and stations that are common in both data types, we computed cross-correlations for time series representative of waveforms and that representative of spectra. The obtained Pearson coefficients are below 0.15 (Table S3, Figs S8–S14) indicating insignificant correlation.

The lune parametrization (Tape & Tape 2015) is utilized to parametrize the moment tensor. This parametrization is a profound advantage for considering CMTs in a Bayesian framework since prior specification becomes intuitively straightforward and the parametrization permits changing the MT model constraints simply

by limiting the prior for some parameters (e.g. limiting the MT to only consider DC mechanisms).

Simulation cases demonstrated the method's capability and reliability. For field data, we demonstrated the method for the largest event in the study area where many high SNR waveforms are available and other published solutions exist. The results show that joint inversion can resolve the CMT with just a single waveform complemented with spectra and polarities to comparable uncertainty as the reference solution based on 40 waveforms. Results for a  $M_L$  2.5 event show similar results. Finally, results for 10 events in the region show robust results to  $M_L$  1.6. Estimates of CMTs for all events indicate predominant strike slip focal mechanisms with low CLVD and low isotropic components. Shallow depths are resolved for all events, and source durations appear to be reasonably resolved.

Overall, we observed that incorporating amplitude spectra at intermediate frequencies significantly reduces model parameter uncertainties. In addition, polarity data resolve the focal mechanism which, in turn, helps reducing uncertainties for the centroid and STF parameters.

## SUPPORTING INFORMATION

Supplementary data are available at *GJI* online.

### suppl.data

Please note: Oxford University Press is not responsible for the content or functionality of any supporting materials supplied by the authors. Any queries (other than missing material) should be directed to the corresponding author for the paper.

## ACKNOWLEDGMENTS

We acknowledge the Microseismic Industry Consortium and Nanometrics for their support and contribution, including the installation and maintenance of stations. Plots were produced with Matplotlib and the Generic Mapping Tools (e.g. Hunter 2007; Wessel *et al.* 2013). This work used the open source library pyrocko (Heimann *et al.* 2019) and the Bayesian Earthquake Analysis Tool (BEAT, Vasyura-Bathke *et al.* 2020). All methods presented in this work are available for use in the current release of BEAT.

## DATA AVAILABILITY

Seismic data and station metadata can be downloaded directly from the Incorporated Research Institutions for Seismology (IRIS) website (<https://ds.iris.edu/wilber3/>), and the earthquake catalogue is provided by Nanometrics. This work is funded by NSERC Alliance Grant ALLRP 548576-2019 entitled 'Dynamics of fault activation by hydraulic fracturing: Insights from new technologies', with partners ARC Resources, Ltd., Canadian Natural Resources Limited, ConocoPhillips Canada, Ovintiv, Tourmaline Oil Corp. Geoscience BC, Nanometrics and OptaSense. The following seismic networks were used for the moment tensor inversion: 1E2018, XL2017, PQ2013, EO2018.

## REFERENCES

- Aki, K. & Richards, P.G., 2002. *Quantitative Seismology*, 2nd edn, University Science Books.
- Alvizuri, C. & Tape, C., 2016. Full moment tensors for small events ( $M_w < 3$ ) at Uturuncu volcano, Bolivia, *Geophys. J. Int.*, **206**(3), 1761–1783.
- Barclay, J., Krause, F., Campbell, R. & Utting, J., 1990. Dynamic casting and growth faulting: Dawson Creek graben complex, Carboniferous–Permian Peace River embayment, western Canada, *Bull. Can. Petrol. Geol.*, **38**(1), 115–145.
- Brillinger, D., Udias, A. & Bolt, B., 1980. A probability model for regional focal mechanism solutions, *Bull. seism. Soc. Am.*, **70**(1), 149–170.
- Cesca, S., Buforn, E. & Dahm, T., 2006. Amplitude spectra moment tensor inversion of shallow earthquakes in Spain, *Geophys. J. Int.*, **166**(2), 839–854.
- Cesca, S., Grigoli, F., Heimann, S., Dahm, T., Kriegerowski, M., Sobiesiak, M., Tassara, C. & Olcay, M., 2016. The  $M_w$  8.1 2014 Iquique, Chile, seismic sequence: a tale of foreshocks and aftershocks, *Geophys. J. Int.*, **204**(3), 1766–1780.
- Cesca, S., Heimann, S., Stammer, K. & Dahm, T., 2010. Automated procedure for point and kinematic source inversion at regional distances, *J. geophys. Res.*, **115**(B6), doi:10.1029/2009JB006450.
- De Matteis, R., Convertito, V. & Zollo, A., 2016. BISTROP: Bayesian inversion of spectral-level ratios and P-wave polarities for focal mechanism determination, *Seismol. Res. Lett.*, **87**(4), 944–954.
- Del Moral, P., Doucet, A. & Jasra, A., 2006. Sequential Monte Carlo samplers, *J. R. Stat. Soc., B*, **68**(3), 411–436.
- Dettmer, J., Dosso, S.E. & Holland, C.W., 2007. Uncertainty estimation in seismo-acoustic reflection travel time inversion, *J. acoust. Soc. Am.*, **122**(1), 161–176.
- Dziewonski, A.M., Chou, T.-A. & Woodhouse, J.H., 1981. Determination of earthquake source parameters from waveform data for studies of global and regional seismicity, *J. geophys. Res.*, **86**(B4), 2825–2852.
- Ekström, G., Nettles, M. & Dziewoński, A., 2012. The global CMT project 2004–2010: centroid-moment tensors for 13,017 earthquakes, *Phys. Earth planet. Inter.*, **200**, 1–9.
- Fichtner, A. & Simutè, S., 2018. Hamiltonian Monte Carlo inversion of seismic sources in complex media, *J. geophys. Res.*, **123**(4), 2984–2999.
- Fox, A.D. & Watson, N., 2019. Induced Seismicity Study in the Kiskatinaw Seismic Monitoring and Mitigation Area, British Columbia, for the BC Oil and Gas Commission, Final Report, Enlighten Geoscience Limited, 51pp.
- Fox, B.D., Selby, N.D., Heyburn, R. & Woodhouse, J.H., 2012. Shallow seismic source parameter determination using intermediate-period surface wave amplitude spectra, *Geophys. J. Int.*, **191**(2), 601–615.
- Geological Survey of Canada, International Federation of Digital Seismograph Networks, <https://www.fdsn.org/networks/detail/PQ/>, 2013..
- Gu, C., Marzouk, Y.M. & Toksöz, M.N., 2018. Waveform-based Bayesian full moment tensor inversion and uncertainty determination for the induced seismicity in an oil/gas field, *Geophys. J. Int.*, **212**(3), 1963–1985.
- Hardebeck, J. & Shearer, P., 2003. Using S/P Amplitude Ratios to Constrain the Focal Mechanisms of Small Earthquakes, *Bull. seism. Soc. Am.*, **93**(6), 2434–2444.
- Hardebeck, J.L. & Shearer, P.M., 2002. A new method for determining first-motion focal mechanisms, *Bull. seism. Soc. Am.*, **92**(6), 2264–2276.
- Heimann, S. *et al.*, 2018. Grond - A probabilistic earthquake source inversion framework. V. 1.0. GFZ Data Services. doi: 10.5880/GFZ.2.1.2018.003.
- Heimann, S., 2011. A robust method to estimate kinematic earthquake source parameters, *PhD thesis*, Staats- und Universitätsbibliothek Hamburg Carl von Ossietzky.
- Heimann, S., Vasyura-Bathke, H., Sudhaus, H., Isken, M.P., Kriegerowski, M., Steinberg, A. & Dahm, T., 2019. A Python framework for efficient use of pre-computed Green's functions in seismological and other physical forward and inverse source problems, *Solid Earth*, **10**(6), 1921–1935.
- Herrmann, R.B., Benz, H. & Ammon, C.J., 2011. Monitoring the earthquake source process in North America, *Bull. seism. Soc. Am.*, **101**(6), 2609–2625.
- Hunter, J.D., 2007. Matplotlib: A 2D graphics environment, *Comput. Sci. Eng.*, **9**(03), 90–95.
- Jaynes, E.T., 2003. *Probability Theory: The Logic of Science*, Cambridge Univ. Press.
- Kühn, D., Heimann, S., Isken, M.P., Ruigrok, E. & Dost, B., 2020. Probabilistic moment tensor inversion for hydrocarbon-induced seismicity in

- the Groningen gas field, the Netherlands, part 1: testing, *Bull. seism. Soc. Am.*, **110**(5), 2095–2111.
- Mahani, A.B., Esfahani, F., Kao, H., Gaucher, M., Hayes, M., Visser, R. & Venables, S., 2020. A systematic study of earthquake source mechanism and regional stress field in the southern Montney unconventional play of northeast British Columbia, Canada, *Seismol. Res. Lett.*, **91**(1), 195–206.
- Mahani, A.B., Schultz, R., Kao, H., Walker, D., Johnson, J. & Salas, C., 2017. Fluid injection and seismic activity in the northern Montney play, British Columbia, Canada, with special reference to the 17 august 2015  $M_w$  4.6 induced earthquake, *Bull. seism. Soc. Am.*, **107**(2), 542–552.
- Malinverno, A. & Briggs, V.A., 2004. Expanded uncertainty quantification in inverse problems: hierarchical bayes and empirical bayes, *Geophysics*, **69**(4), 1005–1016.
- McGill University (Canada), 2017, International Federation of Digital Seismograph Networks *McGill Dawson-Septimus Induced Seismicity Study*, [https://www.fdsn.org/networks/detail/XL\\_2017/](https://www.fdsn.org/networks/detail/XL_2017/).
- Mei, S., 2009. New insights on faults in the Peace River Arch region, northwest Alberta, based on existing well-log data and refined trend surface analysis, *Can. J. Earth Sci.*, **46**(1), 41–65.
- Monelli, D. & Mai, P.M., 2008. Bayesian inference of kinematic earthquake rupture parameters through fitting of strong motion data, *Geophys. J. Int.*, **173**(1), 220–232.
- Mustać, M. & Tkalčić, H., 2016. Point source moment tensor inversion through a Bayesian hierarchical model, *Geophys. J. Int.*, **204**(1), 311–323.
- Natural Resources Canada (NRCAN Canada), 2018. International Federation of Digital Seismograph Networks, *GSC-BCOGC Induced Seismicity Study*, [https://www.fdsn.org/networks/detail/IE\\_2018/](https://www.fdsn.org/networks/detail/IE_2018/).
- Peña Castro, A., Roth, M., Verdecchia, A., Onwumeka, J., Liu, Y., Harrington, R., Zhang, Y. & Kao, H., 2020. Stress chatter via fluid flow and fault slip in a hydraulic fracturing-induced earthquake sequence in the Montney Formation, British Columbia, *Geophys. Res. Lett.*, **47**(14), e2020GL087254, doi:10.1029/2020GL087254.
- Petersen, G.M. *et al.*, 2021. Regional centroid moment tensor inversion of small to moderate earthquakes in the Alps using the dense Alparray seismic network: challenges and seismotectonic insights, *Solid Earth*, **12**(6), 1233–1257.
- Pugh, D., White, R. & Christie, P., 2016. A Bayesian method for microseismic source inversion, *Geophys. J. Int.*, **206**(2), 1009–1038.
- Razafindrakoto, H.N. & Mai, P.M., 2014. Uncertainty in earthquake source imaging due to variations in source time function and earth structure, *Bull. seism. Soc. Am.*, **104**(2), 855–874.
- Rice, S.O., 1944. Mathematical analysis of random noise, *Bell Syst. Tech. J.*, **23**(3), 282–332.
- Salvage, R. *et al.*, 2021. *Real-time monitoring of seismic activity in the Kiskatinaw area, Northeastern British Columbia (NTS 093P, 094A)*, Tech. rep., Geoscience BC Summary of Activities 2020: Energy and Water.
- Salvage, R.O. & Eaton, D.W., 2022. The influence of a transitional stress regime on the source characteristics of induced seismicity and fault activation: evidence from the 30 November 2018 Fort St. John  $M_L$  4.5 induced earthquake sequence, *Bull. seism. Soc. Am.*, **112**(3), 1336–1355.
- Shang, X. & Tkalčić, H., 2020. Point-source inversion of small and moderate earthquakes from P-wave polarities and P/S amplitude ratios within a hierarchical Bayesian framework: implications for the Geysers earthquakes, *J. geophys. Res.*, **125**(2), e2019JB018492, doi:10.1029/2019JB018492.
- Snoke, J.A., Lee, W., Kanamori, H., Jennings, P. & Kisslinger, C., 2003. 85.12 FOCMEC: FOCal MECHANism determinations, in *International Handbook of Earthquake and Engineering Seismology*, Vol. **81**, Part B, pp. 1629–1630, eds Lee, William H.K., Kanamori, H., Jennings, P.C. & Kisslinger, C., Elsevier Inc.
- Stähler, S.C. & Sigloch, K., 2014. Fully probabilistic seismic source inversion—Part 1: efficient parameterisation, *Solid Earth*, **5**(2), 1055–1069.
- Tape, W. & Tape, C., 2015. A uniform parametrization of moment tensors, *Geophys. J. Int.*, **202**(3), 2074–2081.
- Tarantola, A., Valette, B. *et al.*, 1982. Inverse problems = quest for information, *J. Geophys.*, **50**(1), 159–170. <https://n2t.net/ark:/88439/y048722>.
- Tarantola, A. & Valette, B., 1982. Generalized nonlinear inverse problems solved using the least squares criterion, *Rev. Geophys.*, **20**(2), 219–232. University of Calgary (U of C Canada). 2018 *EON-ROSE International Federation of Digital Seismograph Networks* <https://www.fdsn.org/network/detail/EO/>
- Vackář, J., Burjánek, J., Gallovič, F., Zahradník, J. & Clinton, J., 2017. Bayesian ISOLA: new tool for automated centroid moment tensor inversion, *Geophys. J. Int.*, **210**(2), 693–705.
- Valentine, A.P. & Woodhouse, J.H., 2010. Reducing errors in seismic tomography: combined inversion for sources and structure, *Geophys. J. Int.*, **109**(2), 259–274.
- Vasyura-Bathke, H. *et al.*, 2020. The Bayesian earthquake analysis tool, *Seismol. Res. Lett.*, **91**(2A), 1003–1018.
- Vasyura-Bathke, H., Dettmer, J., Dutta, R., Mai, P.M. & Jonsson, S., 2021. Accounting for theory errors with empirical Bayesian noise models in nonlinear centroid moment tensor estimation, *Geophys. J. Int.*, **225**(2), 1412–1431.
- Vavryčuk, V., 2014. Iterative joint inversion for stress and fault orientations from focal mechanisms, *Geophys. J. Int.*, **199**(1), 69–77.
- Walsh, D., Arnold, R. & Townend, J., 2009. A Bayesian approach to determining and parametrizing earthquake focal mechanisms, *Geophys. J. Int.*, **176**(1), 235–255.
- Wang, R., 1999. A simple orthonormalization method for stable and efficient computation of Green's functions, *Bull. seism. Soc. Am.*, **89**(3), 733–741.
- Wéber, Z., 2006. Probabilistic local waveform inversion for moment tensor and hypocentral location, *Geophys. J. Int.*, **165**(2), 607–621.
- Wéber, Z., 2018. Probabilistic joint inversion of waveforms and polarity data for double-couple focal mechanisms of local earthquakes, *Geophys. J. Int.*, **213**(3), 1586–1598.
- Wessel, P., Smith, W.H., Scharroo, R., Luis, J. & Wobbe, F., 2013. Generic mapping tools: improved version released, *EOS, Trans. Am. geophys. Un.*, **94**(45), 409–410.
- Wozniakowska, P., Eaton, D., Deblonde, C., Mort, A. & Haeri Ardakani, O., 2021. Identification of regional structural corridors in the Montney play using trend-surface analysis combined with geophysical imaging, GSC Open File Rep 8814, Natural Resources Canada, 1308pp.
- Yakovleva, T., 2019. Nonlinear properties of the rice statistical distribution: theory and applications in stochastic data analysis, *J. Appl. Math. Phys.*, **7**(11), 2767–2779.
- Zhao, L.-S. & Helmberger, D.V., 1994. Source estimation from broadband regional seismograms, *Bull. seism. Soc. Am.*, **84**(1), 91–104.